Physicochem. Probl. Miner. Process., 55(4), 2019, 879-895

http://www.journalssystem.com/ppmp

Physicochemical Problems of Mineral Processing

ISSN 1643-1049

Received September 26, 2019; reviewed; accepted January 06, 2019

Study of flow behaviour in a three products hydrocyclone screen: numerical simulation and experimental validation

Chuanzhen Wang [1,2], Jianzhong Chen [1], Lijuan Shen [1], Linhan Ge [2]

[1] Key Laboratory of Coal Processing and Efficient Utilization, Ministry of Education, School of Chemical Engineering and Technology, China University of Mining & Technology, Xuzhou, Jiangsu 221116, China

[2] Discipline of Chemical Engineering, School of Engineering, University of Newcastle, Callaghan, NSW 2308, Australia

Correspondence: jzchen518@126.com (J.Z.C), faxofking@cumt.edu.cn (C.Z.W)

Abstract: A novel three products hydrocyclone screen (TPHS) has been successfully developed; it consists of a cylindrical screen embedded in a conventional hydrocyclone (CH). In the new liquid cyclone, the combination of centrifugal classification and screening was employed for particle separation based on size. The aim of this study is to investigate the flow behaviour in TPHS using numerical simulation and experimental validation. A computational fluid dynamics simulation with a 4.35 million grid scheme and linear pressure–strain RSM generated the economic and grid-independence solution, which agreed well with the experiments of particle image velocimetry and water split. The velocity vector profile reveals that TPHS represented similar flow patterns to CH, wherein in addition to the outer downward swirl flow, inner upward swirl flow, central down-flow, second circulatory flow, and mantle, a particular fluid flow named screen underflow was created in TPHS owing to the presence of a cylindrical screen. The velocity distribution demonstrates that in TPHS, relative to CH, with the increase in radius, the lower tangential and higher radial velocity first increased to a peak and subsequently decreased, while the axial velocity primarily reduced to zero, increased in the opposite direction, and finally decreased rapidly to zero again. In addition, a disadvantageous flow, namely, screen backflow, was generated in TPHS, wherein the farther away the flow is from the feed inlet, the earlier this flow behaviour occurred. However, the rational scheme of aperture size and screen length can completely remove the screen backflow in TPHS.

Keywords: three products hydrocyclone screen, flow behaviour, Computational Fluid Dynamics, particle image velocimetry, water split

1. Introduction

Hydrocyclones are well known as an essential group of equipment for solid–liquid separation in the centrifugal force field (Svarovsky and Thew, 1992; Vieira et al., 2010). The conventional hydrocyclone (CH) consists of one tangential inlet stream (feed) and two axial product streams, comprising a small one at the bottom for discarding coarse particles (underflow) and a large one at the top for discarding fine particles (overflow) (Bradley, 2013). Distinct advantages, such as simple design, flexible performance index operation, high capacity, and low cost, render hydrocyclones as the preferred option in chemical processing (Chu et al., 2004), mineral processing (Awais et al., 2017; Chen et al., 2017), environmental (Li et al., 2016), and some other industries (Wasilewski, 2016). However, the device performance of CHs is attenuated by not only some new tendencies (such as the reduction in the processed particle size (Santana et al., 2008; Vieira and Barrozo, 2014)), but also by inherent disadvantages (such as the unsatisfactory efficiency and sharpness (Chu et al., 2004) and the fish-hook effects (Dueck et al., 2014; Roldan-Villasana et al., 1993)). Nevertheless, hydrocyclones failed to satisfy some requirements in engineering applications (Mainza et al., 2006). Thus, the CH has undergone some alterations to obtain better performances, for instance, the change in its original structure (Chu et al., 2000; Li et al., 2015;

DOI: 10.5277/ppmp19008

Motin and Bénard, 2017; Niazi et al., 2017; Yoshida et al., 2008) or the introduction of new structures (Hwang et al., 2013; Obeng and Morrell, 2003; Vieira et al., 2016).

According to the aforesaid defects of hydrocyclones, a new three products hydrocyclone screen (TPHS) (Chinese patent number: ZL201020108608.3) has been designed at the Key Laboratory of Coal Processing and Efficient Utilization, China. In this new liquid cyclone shown in Fig. 1, a cylindrical screen was embedded in the CH. The operating principle of the new design can be considered as the combination of centrifugal classification and screening. Three different separation processes, i.e. cylinder stratification, cylinder classification, and cone classification were adopted to separate particles depending on size. The operation of TPHS is analogous to that of CH; however, in addition to the overflow and underflow, TPHS generates a new product stream, namely screen underflow owing to a cylindrical screen addition. In TPHS, the fish-hook effect can be removed entirely, as the entrained and trapped fines in underflow are reduced significantly. Both pilot-scale and industrial-scale experiments indicated that TPHS yields better performances than CHs, such as higher classification efficiency, lower imperfection, and more reasonable cut size. The successful application of TPHS replacing CHs in coal preparation plants indicated its advantage and application potential (Jianzhong et al., 2016; Wang et al., 2018; Zhu et al., 2012).

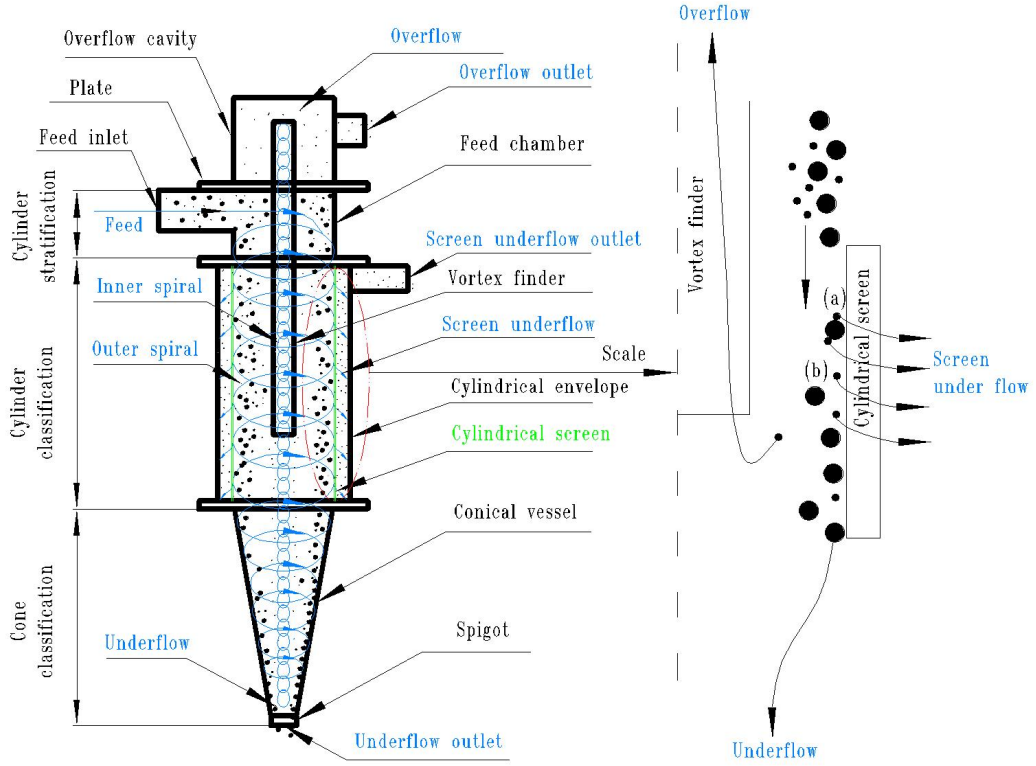

Fig. 1. Schematic diagram of the three products hydrocyclone screen (TPHS)

Despite the simple structure and operation of CHs, the exhaustive mechanisms by which they work are complicated (Chu et al., 2002; Chu et al., 2004; Svarovsky and Thew, 1992). In CHs, the fluid presents complex flow characteristics, for instance, swirling turbulence, flow inversion, vortex breakdown, etc. (Gupta et al., 2008; Hararah et al., 2010; Liu et al., 2014; Wang and Yu, 2006). Given the operational and structural similarities between the conventional and new hydrocyclones, the internal flow in TPHS is identically intricate and of complex mathematical calculation. The performance predictions of TPHS generally depend on empirical models (Wang et al., 2018) that are limited by the restrictions of experimental conditions. This results in the prohibitions of in-depth insight and further extension for TPHS. Thus, given these disadvantages, mathematical models based on fluid dynamics are highly required to explicitly describe the flow characteristics of TPHS.

Computational fluid dynamics (CFD) is a versatile tool to investigate the fluid mechanics of physical systems (Anderson and Wendt, 1995; Hirsch, 2007; Karniadakis and Sherwin, 2013; Salem-Said et al.,

2013). In recent years, owing to the prodigious advances in computational technology, CFD has been used extensively in modelling fluid flows in hydrocyclones. Previous simulation studies (Bhaskar et al., 2007; Cullivan et al., 2004; Narasimha et al., 2005; Schuetz et al., 2004) using the incompressible Navier–Stokes (N–S) equations supplemented by apposite turbulence models have been established as appropriate for modelling the fluid flows of hydrocyclones. Further, the preferred turbulence models typically include the *k*-ε model (Fredriksson, 1999; Griffiths and Boysan, 1996), Reynolds stress model (RSM) (Ghodrat et al., 2016; Parvaz et al., 2017), and large eddy simulation (LES) (Ghadirian et al., 2015; Vakamalla and Mangadoddy, 2017). Nevertheless, the *k*-ε model demonstrates poor agreement with the experimental results owing to its isotropic nature (Balestrin et al., 2017; Mousavian and Najafi, 2009), while LES is limited by high-performance computing and resolution requirements (ANSYS, 2012). Thus, the RSM is typically used to model the flow of hydrocyclones (Mousavian and Najafi, 2009; Swain and Mohanty, 2013; Wang et al., 2007; Zhen-Bo et al., 2011). The application of CFD simulations significantly enhances the comprehension of internal fluids and partly alleviates the applied restriction of empirical models (Balestrin et al., 2017; Mainza et al., 2006; Vieira and Barrozo, 2014). Similar to other innovative cyclones (Mainza et al., 2006; Xu et al., 2016), because TPSH is a derivative of hydrocyclones, the numerical approach for CHs can be applied to TPHS.

However, because of the cylindrical screen addition, the fluid of TPHS demonstrates a distinct flow pattern, i.e. screen underflow relative to CHs (Wang et al., 2018). Hence, the validation of numerical results against experimental data is essential. Particle image velocimetry (PIV) (Hoque et al., 2016) as a non-intrusive visualisation experimental technique has been employed gradually to validate the turbulence model for hydrocyclones (Fan et al., 2015; Liu et al., 2006; Liu et al., 2007; Marins et al., 2010; Wang et al., 2016). This technique creates the flow velocity using the instantaneous 'snapshots' of the fluid flow to describe the unsteady motion of flows accurately. Additionally, a water split test can be used for the numerical validation (Bhaskar et al., 2007), which is defined as the weight percentage of water from the feed stream to product stream.

The discussion of previous works above indicates that some general understanding of TPHS is available; however, the details of fluid flow in TPHS were not reported and remain unexplored. In view of the aforesaid knowledge gap, new studies considering numerical simulation and experimental validation were developed involving a laboratory-scale TPHS. To achieve this aim, PIV and water split experiments were conducted to validate the turbulence models; subsequently, CFD simulations using incompressible N–S equations were employed to investigate the flow behaviour of TPHS. Specifically, the objectives of this work are as follows:

1) explicitly utilise the economical grid-independence scheme and the exact numerical model for TPHS by the comparison of the PIV experiment, water split test, and CFD simulation.

2) comprehensively describe the fluid flow including the vector and distribution of velocity in TPHS using the numerical result.

3) critically analyse the profile and adjustment of the potentially disadvantageous flow pattern in TPHS according to the simulation.

2. Methodology

2.1. Experimental

Figure 2 shows the (a) schematic diagram and (b) photograph of the experimental rig used for the PIV experiments. It comprises two subsystems, i.e. the measured TPHS subsystem and the PIV measuring subsystem. In a measured subsystem, a laboratory-scale TPHS (see Table 1 for details) was conducted in the present work. A 0–12 m^3/h variable speed pump driven by a 3-kW motor and a frequency converter was used to adjust the feed flow, while a flowmeter and a manometer were used to measure the inlet mass flow rate and pressure, respectively. It is noteworthy that a water-filled cube shell surrounds the TPHS to eliminate the light refraction from the cylindrical column. Plexiglas with good optical transparency was fabricated for the TPHS and cube shell. The PIV measuring subsystem (Dantec Dynamics 2D3C DC) includes a double-pulsed laser, a charge-coupled device (CCD) camera, a synchroniser, and a workstation. The double-pulsed laser was used to generate a laser light sheet that was projected onto the measured plane of the TPHS. White seeding particles made of fluorescent polymer (10 μm diameter and 1.05 g/cm^3 density) were illuminated by the laser light sheet, and the

flow field was captured by the CCD camera. A synchroniser was employed to acquire the synchronous image of the CCD camera and double-pulse laser.

Table 1. Structure parameters of laboratory-scale TPHS

Items	**PIV test**
Diameter of cylindrical screen	75 mm
Aperture size	0.7 mm
Thickness of screen bar	5 mm
Width of screen bar	3.25 mm
Length × Width of inlet	29 mm × 8 mm
Length of feed chamber	70 mm
Length of cylindrical envelope	185 mm
Length of vortex finder	300 mm
Diameter of vortex finder	25 mm
Diameter of screen underflow outlet	30 mm
Angle of cone	20°
Diameter of spigot	10 mm

The experimental procedure of PIV was designed as a step-by-step implementation. In step 1, deionised water was transported to the TPHS at an appropriate inlet velocity of 5 ± 0.2 m/s considering the safety of the Plexiglas TPHS; subsequently, three-product streams namely overflow, screen underflow, and underflow were generated. The duration of the measured operating TPHS subsystem was approximately 20 min to achieve steady-state conditions; thereafter, all the outlets were sampled simultaneously to estimate the water split.

In step 2, amounts of seeding particles were blended into the feed tank and dispersed homogeneously. Subsequently, a laser light sheet capable of carrying a 300 mJ/pulse at a trigger rate of 10 Hz was used for the camera shooting. To provide the accurate velocity value, 50 image pairs were captured at the trigger time of 60 μs for the laser and the exposure time of 6000 μs for the camera. It is noteworthy that owing to the screen, while the horizontal plane in the cylindrical section was illuminated, the light in this area could be divided into two parts, i.e. some laser directly passing through the aperture and the remainder refracted by the screen bar. This led to different refractions in this region, which could increase the experimental errors. Thus, the measured area was covered by the CCD camera from x = –37.5 mm to 37.5 mm in the z = 0 plane (see the red area in Fig. 2) in this study, which allowed the laser light sheet to merely pass through the aperture. This demonstrates that only the radial and axial velocities could be detected in the present PIV experiments.

In step 3, the cross correlation between every pair was analysed using the Dynamic Studio software (DYNAMICS, 2011) to generate an instantaneous velocity. Finally, the final velocity was obtained using the average velocity of 50 image pairs.

2.2. Numerical

In this work, the dimensions of the TPHS in the CFD simulation were the same as those in the PIV test. Figure 3 presents the three-dimensional structure grid scheme: (a) side view, and (b) prepared by the hexahedral meshing tool ICEM for the laboratory-scale TPHS, which was divided into three blocks, i.e. cylindrical envelope, cylindrical screen, and CH. The overlaps between the adjacent blocks were merged using the method of mesh interfaces in Fluent. It is clear that the grid was finer in the vicinity of the wall and screen than in the remainder of the TPHS. The maximum cell skewness was below 0.8, and is an excellent grid quality. Three different grid schemes, namely coarse, medium, and fine grids were performed to verify the grid independence (see section 3.1 for details).

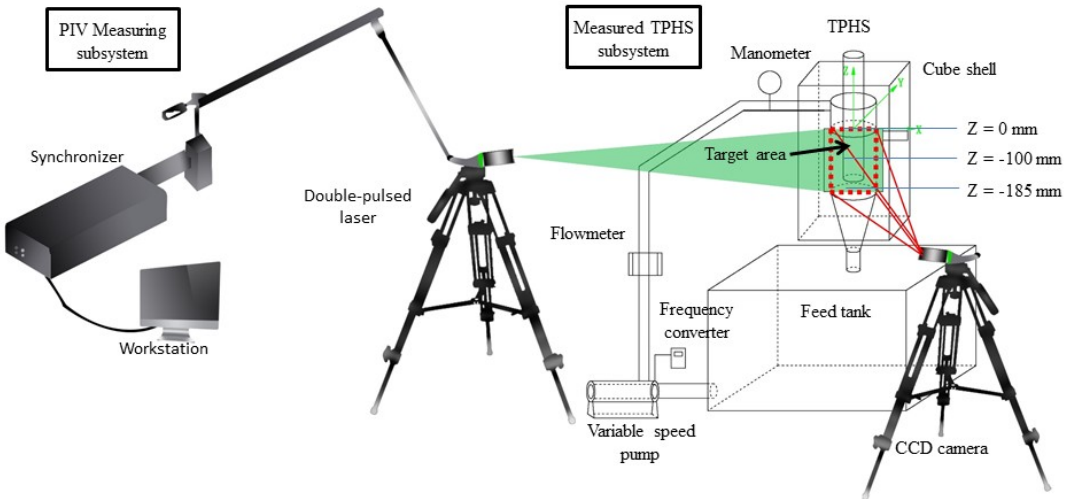

(a)

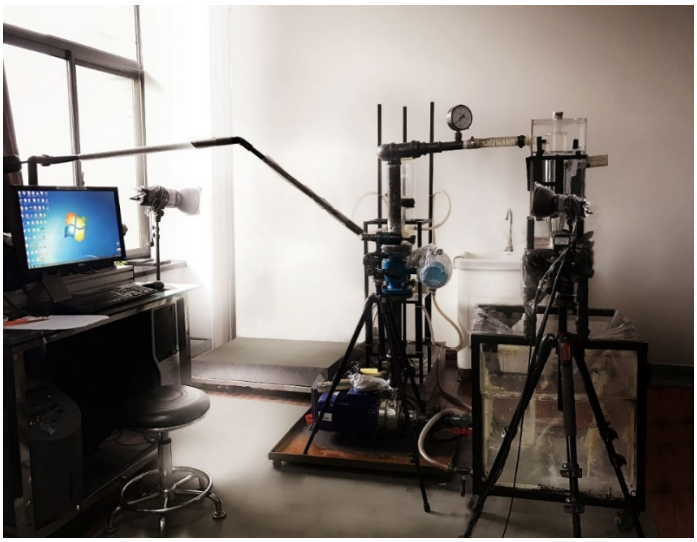

(b)

Fig. 2. Experimental rig of PIV experiments: (a) schematic diagram and (b) photograph

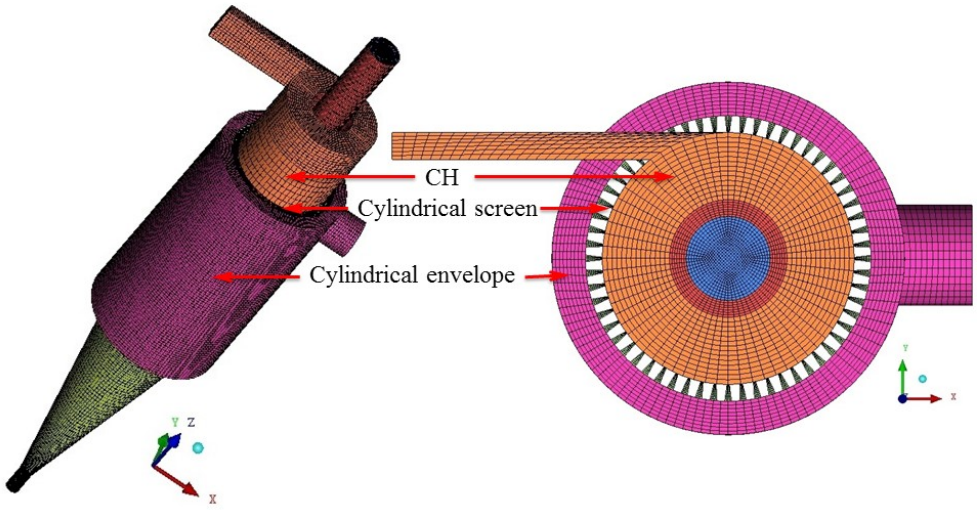

(**a**) (**b**)

Fig. 3. Grid profile of TPHS (a) side view and (b) vertical view

In all the present simulations, two-phase flows using water and air as fluid were modelled by the volume of fluid (VOF) method (Hirt and Nichols, 1981), while the fluid flow was described by the RSM (Gibson and Launder, 1978; Launder et al., 1975; Launder, 1989a). The standard wall function was conducted to model the mean velocity in the near-wall region. The details of the numerical models are shown in Table 2.

Table 2. Multiphase and turbulence models for TPHS simulation

Items	**Models**	
VOF equation:	$\frac{1}{\rho_q}\left[\frac{\partial}{\partial t}\left(\alpha_q\rho_q\right)+\nabla\cdot\left(\alpha_q\rho_q\overset{\mathrm{r}}{u}_q\right)=\sum_{p=1}^{n}\left(\dot{m}_{pq}-\dot{m}_{qp}\right)\right]$	(1)
Turbulence model		
Velocity:	$u_i=\overline{u_i}+u_i'$	(2)
Continuity equation:	$\frac{\partial\rho}{\partial t}+\frac{\partial\rho}{\partial x_i}\left(\rho u_i\right)=0$	(3)
Motion equation:	$\frac{\partial}{\partial t}\left(\rho u_i\right)+\frac{\partial}{\partial x_j}\left(\rho u_i u_j\right)=-\frac{\partial p}{\partial x_i}+\frac{\partial}{\partial x_j}\left[\mu\left(\frac{\partial u_i}{\partial x_j}+\frac{\partial u_j}{\partial x_i}\right)\right]+\frac{\partial}{\partial x_j}\left(-\rho\overline{u_i'u_j'}\right)$	(4)
RSM models:	$\frac{\partial}{\partial t}\left(\rho\overline{u_i'u_j'}\right)+\frac{\partial}{\partial x_k}\left(\rho u_k\overline{u_i'u_j'}\right)$ $=-\frac{\partial}{\partial x_k}\left[\rho\overline{u_i'u_j'u_k'}+\overline{p'\left(\delta_{kj}u_i'+\delta_{jk}u_j'\right)}\right]-\rho\left(\overline{u_i'u_k'}\frac{\partial u_j}{\partial x_k}+\overline{u_j'u_k'}\frac{\partial u_i}{\partial x_k}\right)$ $+\overline{p'\left(\frac{\partial u_i'}{\partial x_j}+\frac{\partial u_j'}{\partial x_i}\right)}-2\mu\overline{\frac{\partial u_i'}{\partial x_k}\frac{\partial u_i'}{\partial x_k}}$	(5)
Standard wall function	$\frac{U_P 0.09^{1/4}k_P^{1/2}}{\tau_w/\rho}=\frac{1}{0.4187}\ln\left(9.793\frac{\rho 0.09^{1/4}k_P^{1/2}y_P}{\mu}\right)$	(6)

In the simulation for TPHS, the boundary condition of the inlet and outlets were defined as the velocity inlet and pressure outlet, respectively. The inlet velocity with the magnitude of 5–15 m/s was normal to the inlet boundary, and the pressure at each outlet was equal to the ambient atmospheric pressure, i.e. 1 atm. The SIMPLEC algorithm was employed as the pressure–velocity coupling scheme for an accurate solution. The schemes of the PRESTO! and second-order upwind was used for the pressure and momentum discretisation, respectively. The standard initialisation was initialised with the air volume fraction of one for all zones. The simulations were conducted by the unsteady solver with a 0.001-s time step in the commercial software ANSYS Fluent 14.5 at the High-Performance Computing Cluster in University of Newcastle, Australia. Sixteen CPUs were assigned to each simulation. Each case was performed for approximately 120 h to consider the physical time of 20 s. All the simulation results shown were averaged over the last 5 s (i.e. 15–20 s), when the simulated fluid flow obtained a steady state, and hence the macroscopic flow characteristics remained stable with time.

3. Results and Discussion

Prior to the CFD simulation to investigate the fluid flow in the TPHS, the validations of the grid scheme and mathematical model were performed. Following this, the flow characteristics including the vector and distribution of velocity were described comprehensively. Subsequently, the potential disadvantage was analysed critically. Despite containing no particles, valuable flow information was obtained. The details are described as follows.

3.1. Validation

The aforesaid grid schemes were utilised to verify the grid independence at the inlet velocity of 5 m/s, wherein the numbers of hexahedral grids were fine ≈ 4.35 million, medium ≈ 2.36 million, and coarse ≈ 0.72 million. All the grid verification simulations were performed using the linear pressure–strain RSM (L_RSM), which is detailed and compared with the stress–Omega RSM (S_RSM) in the next paragraph. Figure 4 shows the distribution of the (a) tangential, (b) axial, and (c) radial velocity at z = –100 mm in the y = 0 plane (see the middle region of the cylindrical section in Fig. 2a). It is noteworthy that the radial position (r) was normalised by the radius of the cylindrical screen (R = 37.5 mm). Further, two gaps occurred in the range of approximately $0.33 < r/R < 0.47$ and $-0.33 < r/R < -0.47$ in each figure, which can be ascribed to the wall of the vortex finder. It is clear that the fine and medium grid schemes present the close distribution of the tangential, axial, and radial velocities, while the obvious divergence can be observed in the coarse grid. This reveals that both the fine and medium grid schemes created the grid-independence solution. However, the finer the grid, the more expensive is the calculation; thus, the medium grid scheme was adopted for the following simulations.

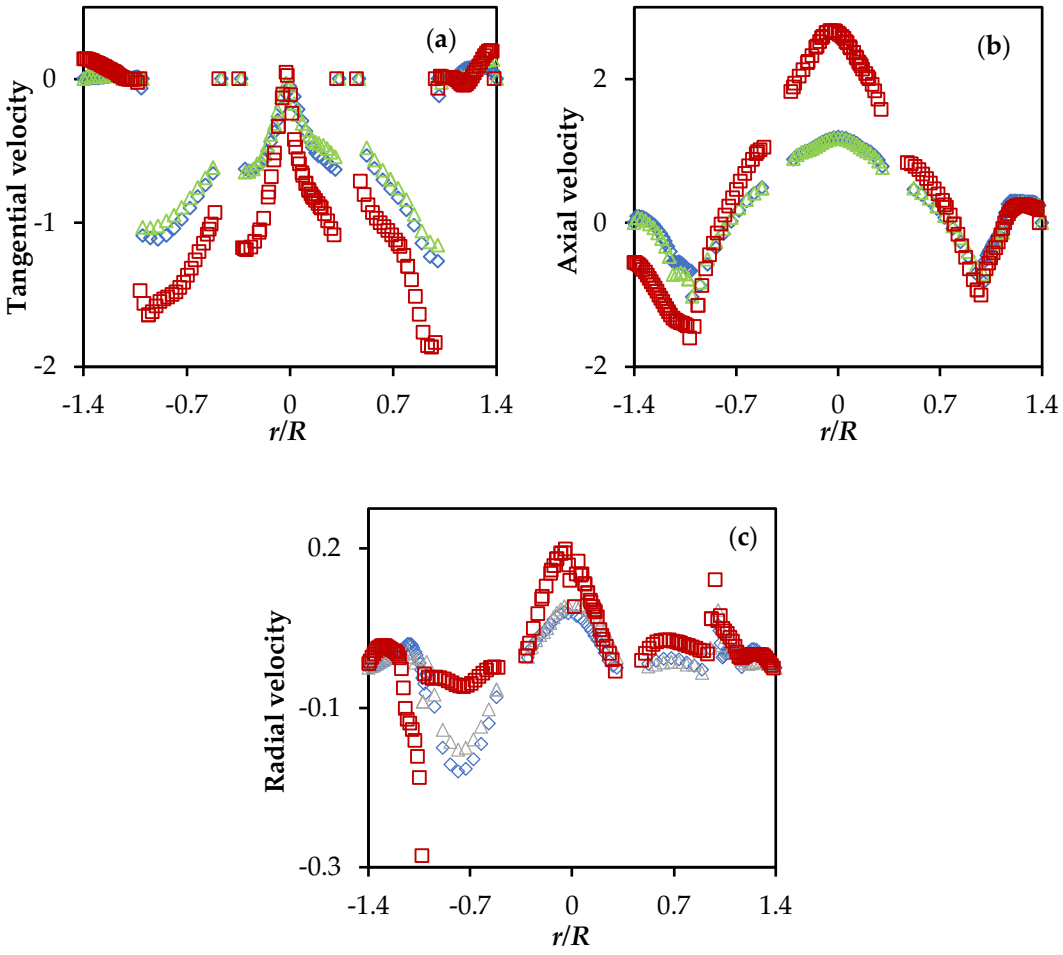

Fig. 4. Comparison of (a) tangential, (b) axial and (**c**) radial velocity (m/s) in CFD simulation using different grid schemes: ◇ Fine △ Medium □ Coarse at z = –100 mm in y = 0 plane

In the present study, the validation of a turbulence model against the experimental data are conducted, and two different types of RSMs are compared, i.e. the L_RSM (Fu et al., 1987; Gibson and Launder, 1978; Launder, 1989b) and S_RSM (Wilcox, 1998) that are based on the dissipation rate (ε) and the specific dissipation rate (ω) equation, respectively. Figure 5 shows the experimental and numerical comparisons of the (a) axial and (b) radial velocity profiles at z = –100 mm (near the middle of cylindrical screen) in the y = 0 plane, and the (c) water split. In Figs. 5a and 5b, the radial and axial velocities

obtained from the simulation demonstrate good agreement with those obtained from the PIV experiment. Additionally, the numerical water split of each product stream (namely underflow, overflow, and screen underflow) is close to the experimental results in Fig. 5c. From Figs. 5a–c, it is evident that a slight difference exists in the flow prediction between L_RSM and S_RSM, probably owing to the sufficient refined grid. This result demonstrates that both L_RSM and S_RSM can predict the characteristic of fluid flows in TPHS well. However, owing to the higher computational stability and lower numerical cost (Balestrin et al., 2017), L_RSM was utilised in the following investigation.

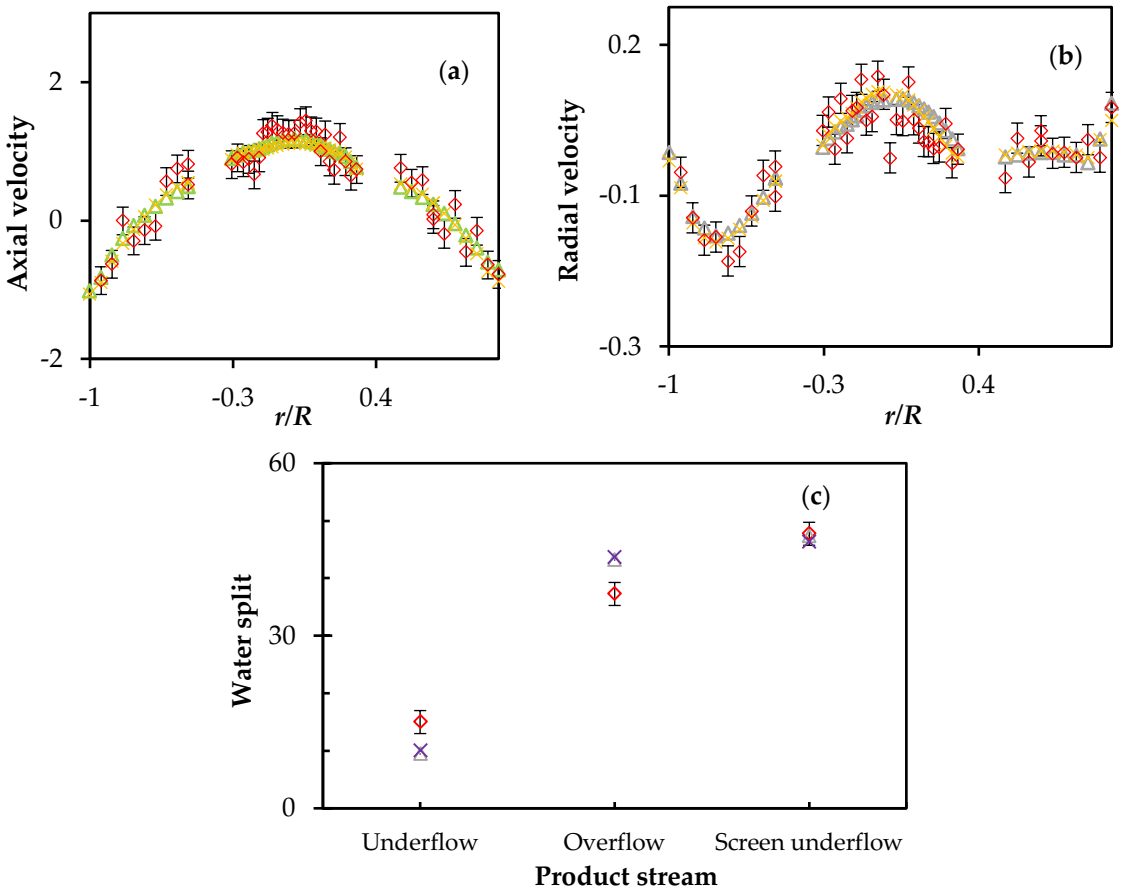

Fig. 5. Comparison between experimental and numerical results of (a) radial velocity and (b) axial velocity (m/s) profile along radius at z = –100 mm in y = 0 plane and (c) water split (%), ▵ L_RSM ×S_RSM ◇ Experimental

3.2. Flow characteristic in TPHS

3.2.1. Velocity vector

Figure 6 shows the velocity vector of the TPHS in the y = 0 plane at the inlet velocity of 10 m/s. Compared to CHs (Bergström and Vomhoff, 2007; Bradley, 2013; Svarovsky and Thew, 1992), the TPHS presents partially similar flow patterns, i.e. outer downward swirl flow, inner upward swirl flow, secondary circulatory flow, and central down-flow. These flow behaviours are attributed to the structural and operational similarity between the TPHS and CHs. It is evident that particles are separated by the centrifugal classification, namely the outer and inner swirl flows create the opposite outward centrifugal and inward drag forces, respectively. The outward centrifugal force governs the coarse particles; thus, they tend to move along the cyclone periphery, join the outer down spiral, and discharge via the underflow outlet. Conversely, the inner drag force dominates the fine particles; hence, they move towards the axial centre, join the inner upward spiral, and flow through the overflow outlet. Additionally, the TPHS presents a particular flow pattern termed screen underflow, as shown in Fig. 6, according to the embedded cylindrical screen. The new pattern demonstrates that the fluid flows via the screen, which creates the outward drag force. Therefore, screening is conducted for the particle classification, i.e. particles smaller than the aperture size could pass across the screen and move to the

screen underflow outlet. The aforesaid outer swirl, inner swirl, and screen underflow indicate the combination of centrifugal classification and screening to separate particles in the TPHS.

However, the local screen underflow in the TPHS exhibits different flow behaviours. From Fig. 6, the left velocity vector directs downward, while the converse direction is observed on the right side. It reveals that the left screen underflow spirals downwards to the right side, merges with the right screen underflow, and moves upwards via the screen underflow outlet. This trend is ascribed to the structural asymmetry caused by the right screen underflow outlet. Further, with the increase in axial depth, the screen underflow exhibits the opposite velocity vector along the radius. For example, in Fig. 6, the velocity vector near z = –20 mm (see the red circle line) directs towards the envelope, while the opposite direction of the velocity vector is obtained near z = –165 mm (see the right green circle line). This implies that the screen underflow flows back to the inside of the screen at the cylindrical bottom. This flow behaviour is named as screen backflow; it allows the fine particles that have been passed through the screen to be dragged by the screen backflow, join the outer spiral, and discharge through the underflow outlet. This not only attenuates the classification efficiency but also consumes energy. It is noteworthy that the initial position of the screen backflow in the left was higher than that in the right (see the green circle line in Fig. 6). More details of the screen backflow are discussed in section 3.3.

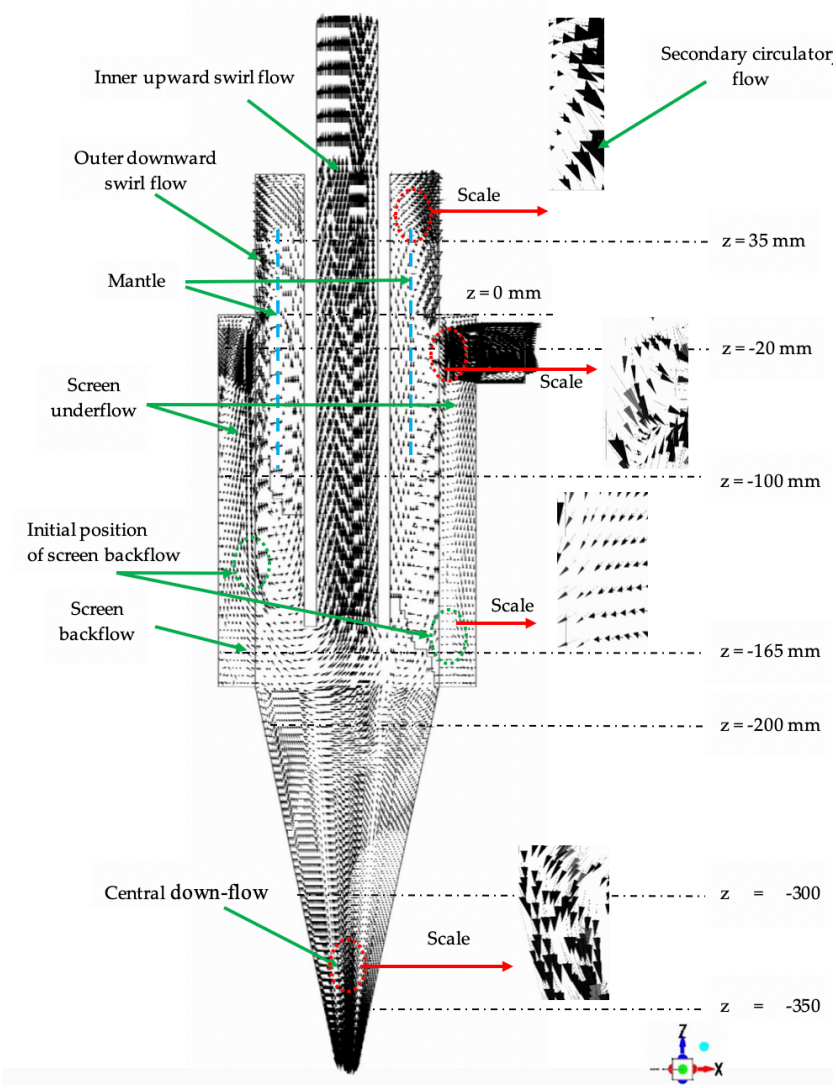

Fig. 6. Distribution of velocity vector in y = 0 mm plane

3.2.2. Velocity distribution

The (a) tangential, (b) axial, and (c) radial velocity distributions of fluid flow along the radius in the TPHS are shown in Figs. 7a–c. The inspection region in the plane y = 0 mm begins at z = 35 mm and

extends deep into the conical vessel to z = –350 mm before the underflow outlet. The lines z = 35 mm and –20 mm are located in the middle of the feed chamber and screen underflow outlet, respectively, while the lines z = –165 mm and –220 mm are located near the interface between the cylindrical and conical sections. The positions z = –100 mm and z = –300 mm are the middle of the cylindrical envelope and conical sections, respectively. It is noteworthy that the position of the zero velocity represents the wall of the vortex finder.

The tangential velocity dominates the fluid flow in a hydrocyclone, and generates the centrifugal force for particle classification (Bergström and Vomhoff, 2007; Bhaskar et al., 2007). Figure 7a shows the tangential velocity in the TPHS. According to the right-hand rule, the clockwise flow in the TPHS (see Figs. 6b–c) results in the negative magnitude. From Fig. 7a, it is evident that the tangential velocity in each horizontal plane presents the similar trend, i.e., with the increase in the radial distance from the axis, the magnitude of the tangential velocity increases to a maximum value at some radial position and subsequently decreases to near 0 m/s. However, the value of the local velocity is significantly different. In detail, as the radius increased, the tangential velocity above the bottom of the vortex finder (see z = 35 and –100 mm in Fig. 7a) increases gradually and decreases rapidly, while below the vortex finder (z = –165 to –350 mm), it increases quickly and decreases steadily. Moreover, with the increase in the vertical depth, the maximum value of the tangential velocity is ~ –2.5 to –0.6 m/s (reduced by ~400%) in the cylindrical section and ~ –0.2 to –0.7 m/s (increased by ~300%) in the conical section. The fluid flow between the cylindrical screen and cylindrical envelope, i.e. the screen backflow, exhibits both positive and negative values that represent the different flow rotations. Compared to CHs (Bhaskar et al., 2007), the TPHS exhibits a lower tangential velocity and can promote fines passing through the screen (Dong and Yu, 2012), but may attenuate the conical classification (Mainza et al., 2006). The characteristic of tangential velocity above reveals the similar trend presented in the TPSH with the exception of the velocity distribution between the cylindrical screen and envelope, which is absent in CHs (Bhaskar et al., 2007; Mainza et al., 2006; Slack and Wraith, 1997).

The axial velocity is an important component responsible for particle separation (Hsieh and Rajamani, 1991; Mainza et al., 2006; Solero and Coghe, 2002). Figure 7b presents the axial velocity in the TPHS. It is clear that reverse vertical flows exist in the TPHS – one traveling upward represented by the positive axial velocity while the other moving downward represented by the negative axial velocity. Furthermore, with increasing radius, the upward axial velocity reduces gradually, and the downward increases to a local maximum and subsequently declines to 0 m/s as the radial distance approaches the wall. The loci of the zero vertical velocity (LZVV) of the TPHS is obtained by lining the point with the vertical velocity of 0 m/s at different vertical heights, which is similar to CHs (Dai et al., 1999). This indicates that the fluid inside the LZVV flowed upward, while the fluid outside the LZVV moved downwards.

A radial displacement gradient is always required for the particle separation; thus, the radial velocity may be the most significant parameter for the separation mechanisms (Bergström and Vomhoff, 2007). The radial velocity component is described in Fig. 6c. It is evident that the radial velocity in the TPHS exhibits the similar trend to the tangential velocity, i.e. the radial velocity increases to a peak and subsequently decreases to 0 m/s near the wall with increasing radius. Moreover, the converse fluid flow along the radial direction is created in a different axial depth. In general, the positive and negative radial velocities are generated, implying the outward and inward fluid flows in the top and bottom, respectively. Relative to the CH (Quian et al., 1989), the TPHS with the converse flow in the top of the cylindrical section exhibits a higher radial velocity, which is attributed to the cylindrical screen. This flow characteristic can result in the distinct outward drag force to promote fines passing through screen in the top, and the inward drag force to govern the fines to join in the inner swirl flow. In addition, the direction change of the radial velocity from outward to inward with increasing axial depth reveals the screen backflow mentioned above (see section 3.2.1).

3.3. Screen backflow

As mentioned above, because the screen backflow is a potential disadvantage of the TPHS, it needs to be removed for better device performance. Thus, more CFD simulations at different boundary conditions and geometry structure were performed to investigate the regularity of screen backflow. To

quantify this flow behaviour, the initial position of the screen backflow (hereinafter referred to as initial position) was defined, thus implying that the backflow merely exists below this position. The smaller the absolute value, the shallower is the initial position, namely the earlier the screen backflow appears. Figure 8 shows the distribution of the initial position with the increasing position angles (0–360°) in the TPHS at different inlet velocities of 5, 8, 10, 12, and 15 m/s. The 0° position angle directs the right direction of the X-axis and rotates clockwise. It is evident that TPHSs with different inlet velocities display the similar trend of the initial position, i.e. the initial position fluctuates with the position angle following the shape of sine curve. Particularly, with the increase in the position angle, the absolute value of the initial position increases. After achieving the maximum value (~140 ± 10 mm), it decreases gradually to a minimum value (~80 ± 10 mm) and subsequently increases again. The deepest and shallowest initial positions are approximately 90° and 270°, respectively. This result represents that the farther away from the feed inlet, the sooner the screen backflow occurs, and vice versa. Further, in Fig. 8, each distribution of the initial position overlaps with the others, thus revealing the insignificant effect of the inlet velocity on the screen backflow.

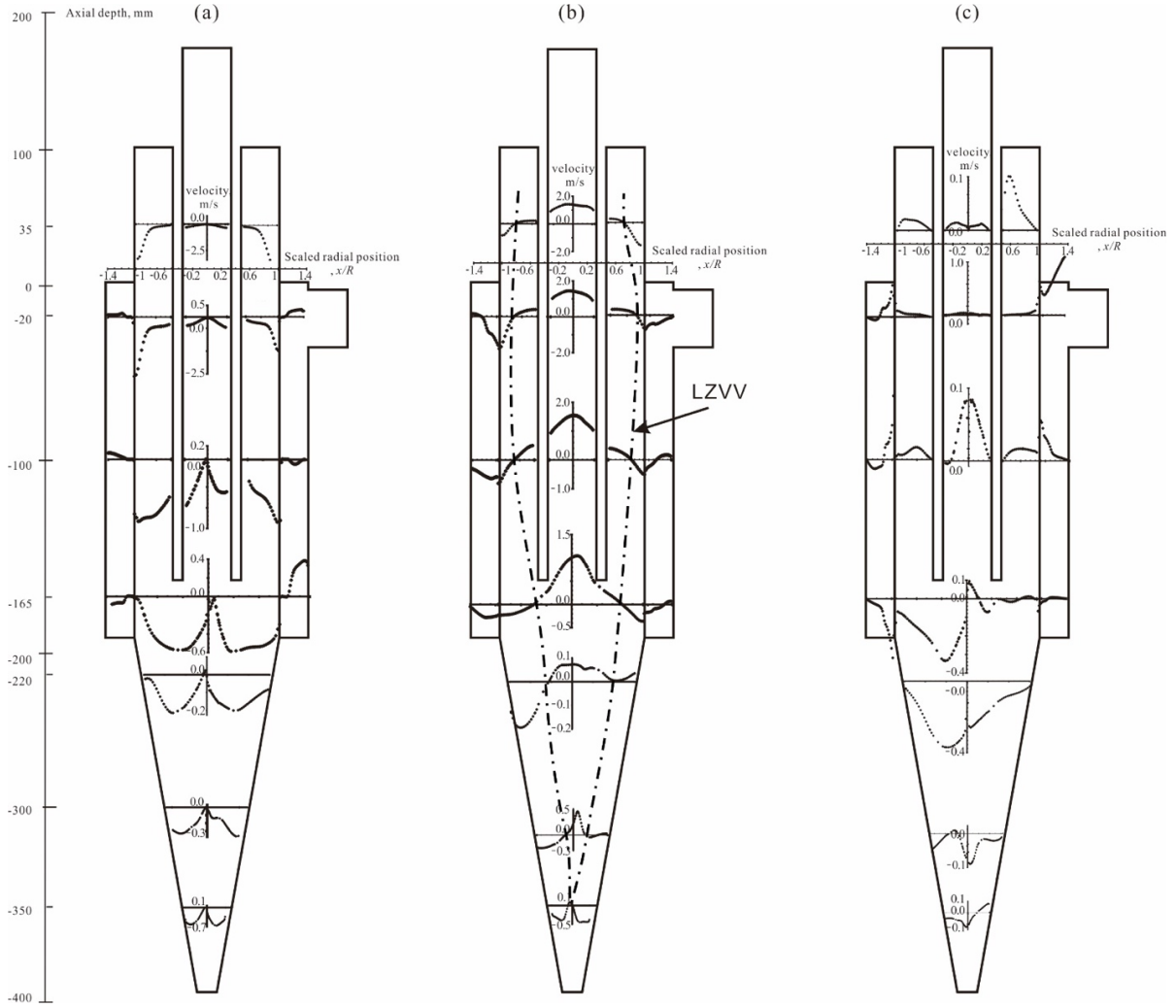

Fig. 7. Velocity distribution in the plane y = 0 mm at different z positions in TPHS: (a) tangential, (b) axial, and (c) radial velocity

Moreover, it is clear that the cylindrical screen is responsible for the flow behaviour of the screen backflow. Thus, different lengths and aperture sizes of the cylindrical screen were considered to analyse their effects on the screen backflow. The maximum backflow ratio was employed for the quantification of the impact, and is defined as the length percentage of backflow accounting for the height of the cylindrical screen at the position angle of 270°. Figure 9 shows the numerical profiles of the maximum backflow ratio with the inlet velocity of 10 m/s: Case 1, where the aperture size changes from 0.4 mm

to 0.8 mm at the screen length of 185 mm; Case 2, where the screen length changes from 75 mm to 185 mm at the aperture size of 0.7 mm. As shown in Fig.9, the maximum backflow ratio reduces until it approaches 0% as the aperture size and length of the cylindrical screen decrease. It is noteworthy that the aperture size of the cylindrical screen is closely related to the target cut size of the particle separation (Wang et al., 2018); thus, the reduction in aperture size to remove the screen backflow should be considered carefully. This result indicates that the rational structural scheme of the aperture size and screen length can attenuate the screen backflow in the TPHS.

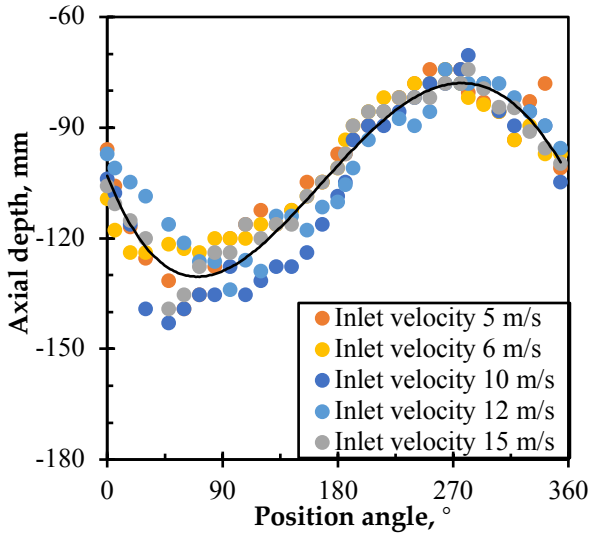

Fig. 8. Distribution of initial position with increasing position angle under different inlet velocities

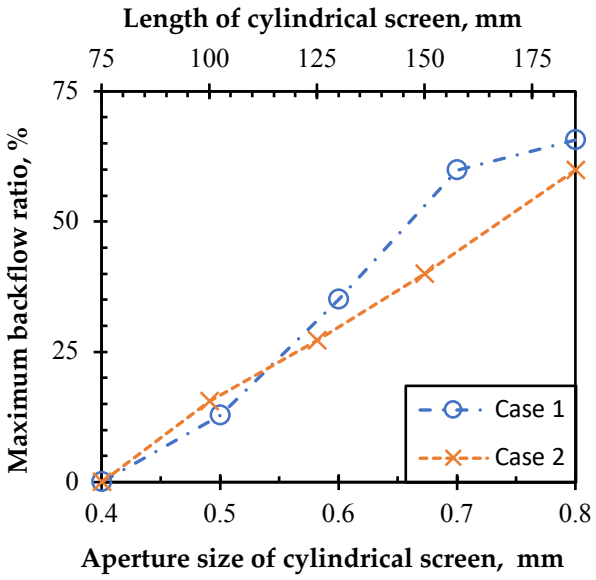

Fig. 9. Maximum backflow ratio obtained by CFD simulation with the inlet velocity of 10 m/s in the TPHS, wherein the aperture size changes at the screen length of 185 mm in Case 1, and the screen length changes at the aperture size of 0.7 mm in Case 2.

4. Conclusion

In the present study, a novel TPHS was successfully developed; it included a cylindrical screen embedded in a CH. A simulation and an experiment were utilised to determine the flow behaviour in the new liquid cyclone. The comparison between numerical and experimental results was used to validate the grid scheme and mathematical model. Based on this, a simulation was performed to

comprehensively investigate the fluid characteristics and critically explore the potentially disadvantageous flow pattern in the TPHS. According to the results and discussion above, the following conclusions were achieved:

1) Comparison of CFD simulations using different gird schemes indicated that the fine (≈4.35 million hexahedral grids) or medium (≈2.36 million hexahedral grids) grids, relative to the coarse grid (≈0.72 million hexahedral grids), could generate the grid-independence solution. However, for the economy of simulation, the medium grid scheme was adopted for the TPHS.

2) Numerical simulations using neither the L_RSM nor the S_RMS could agree well with the experiments of PIV and water spilt. However, the L_RSM was utilised to model the fluid flow in the TPHS owing to its higher computational stability and lower numerical cost.

3) From the profile of velocity vector, the TPHS exhibited similar flow patterns to the CH. In addition to the outer downward swirl flow, inner upward swirl flow, central down-flow, second circulatory flow, and mantle, the TPHS presents a particular flow pattern termed screen underflow owing to the cylindrical screen.

4) Compared to CHs, the lower tangential and higher radial velocity were generated in the TPHS to direct the fine particles passing through screen that first increased to a peak and subsequently decreased as the radius increased. In addition, with the increasing radius, the axial velocity reduced to zero, increased towards the opposite direction, and decreased rapidly to zero again, thus generating the LZVV.

5) At the bottom of the cylindrical screen, the TPHS demonstrated a deficient fluid flow, named screen backflow, whose initial position fluctuated with the position angle following a sine curve. The deepest and shallowest initial positions were approximately 90° and 270°, respectively, indicating that that the farther away from the feed inlet, the sooner the screen backflow occurred, and vice versa. The screen backflow attenuated with the decreasing aperture size and length of the cylindrical screen, except for the weak effect of inlet velocity on this flow behaviour.

In future, based on the present work, attempts to investigate the particle motion in the TPHS will be conducted using the CFD–DEM method.

Acknowledgments:

This work was supported by the "Fundamental Research Funds for The Central Universities", China; the Priority Academic Program Development of Jiangsu Higher Education Institutions, China; the National Natural Science Foundation of China (No. 51574233, 51604273 and 51604196); the Fund of State Key Laboratory of Mineral Processing (BGRIMM-KJSKL-2016-06); the China Postdoctoral Science Foundation (2017M612522); the High-Performance Computing Cluster in the University of Newcastle, Australia.

Appendix A

Nomenclature

$\vec{u}_q$	Velocity vector (m/s)
$\bar{u}$	Mean velocity component (m/s)
u'	Fluctuation velocity component (m/s)
i, j	x, y or z components
p, q	Phase in fluid
a_q	the q^{th} fluid's volume fraction in the cell
$\dot{m}_{pq}$ ($\dot{m}_{qp}$)	the mass transfer from phase p (q) to phase q (p)
k_P	turbulence kinetic energy at the wall-adjacent cell centroid, P
t	time (s)
U_P	mean velocity of the fluid at the wall-adjacent cell centroid, P

x_i, x_j, x_k	position (m)
y_P	distance from the centroid of the wall-adjacent cell to the wall, P
δ	Kronecker delta function
ρ	density (kg/m^3)
τ_w	wall shear stress

Abbreviations

CCD	charge-coupled device
CFD	computational fluid dynamics
CH	conventional hydrocyclone
LES	Large Eddy Simulation
LZVV	loci of zero vertical velocity
L_RSM	linear pressure–strain RSM
Navier-Stokes	N–S
PIV	particle image velocimetry
RSM	Reynolds stress model
TPHS	three products hydrocyclone screen
S_RSM	stress−Omega RSM
VOF	volume of fluid

References

ANDERSON, J.D., Wendt, J., 1995. *Computational fluid dynamics*. Springer.

ANSYS, 2012. *Fluent version 14.5 users' manual*.

AWAIS, M., COELHO, F., DEGRI, M., HERRAIZ, E., WALTON, A., ROWSON, N., 2017. *Hydrocyclone Separation of Hydrogen Decrepitated NdFeB*. Recycling 2, 22.

BALESTRIN, E., DECKER, R., NORILER, D., BASTOS, J., MEIER, H., 2017. A*n alternative for the collection of small particles in cyclones: Experimental analysis and CFD modeling*. Separation and Purification Technology 184, 54-65.

BERGSTROM, J., VOMHOFF, H., 2007. *Experimental hydrocyclone flow field studies*. Separation and Purification Technology 53, 8-20.

BHASKAR, K.U., MURTHY, Y.R., RAJU, M.R., TIWARI, S., SRIVASTAVA, J.K., RAMAKRISHNAN, N., 2007. *CFD simulation and experimental validation studies on hydrocyclone*. Minerals Engineering 20, 60-71.

BRADLEY, D., 2013. *The Hydrocyclone: International Series of Monographs in Chemical Engineering*. Elsevier.

CHEN, L., YOU, Z., XIE, H., ZHANG, H., LI, Y., WEI, Z., 2017. *Fluidized hydrocyclone for continuous centrifugal concentration*. Separation Science and Technology 52, 1283-1288.

CHU, L.-Y., CHEN, W.-M., LEE, X.-Z., 2002. *Effects of geometric and operating parameters and feed characters on the motion of solid particles in hydrocyclones*. Separation and purification technology 26, 237-246.

CHU, L.-Y., YU, W., WANG, G.-J., ZHOU, X.-T., Chen, W.-M., Dai, G.-Q., 2004. Enhancement of hydrocyclone separation performance by eliminating the air core. Chemical Engineering and Processing: Process Intensification 43, 1441-1448.

CHU, L.Y., CHEN, W.M., LEE, X.Z., 2000. Effect of structural modification on hydrocyclone performance. Separation and Purification Technology 21, 71-86.

CULLIVAN, J.C., WILLIAMS, R.A., DYAKOWSKI, T., CROSS, C.R., 2004. *New understanding of a hydrocyclone flow field and separation mechanism from computational fluid dynamics*. Minerals Engineering 17, 651-660.

DAI, G., CHEN, W., LI, J., CHU, L., 1999. Experimental study of solid–liquid two-phase flow in a hydrocyclone. Chemical Engineering Journal 74, 211-216.

DONG, K., YU, A., 2012. Numerical simulation of the particle flow and sieving behaviour on sieve bend/low head screen combination. Minerals Engineering 31, 2-9.

DUECK, J., FARGHALY, M., NEESE, T., 2014. T*he theoretical partition curve of the hydrocyclone*. Minerals

Engineering 62, 25-30.
DYNAMICS, D., 2011. DynamicStudio v3.20 User's Guide.
FAN, Y., WANG, J., BAI, Z., WANG, J., WANG, H., 2015. E*xperimental investigation of various inlet section angles in mini-hydrocyclones using particle imaging velocimetry*. Separation and Purification Technology 149, 156-164.
FREDRIKSSON, C., 1999. *Exploratory experimental and theoretical studies of cyclone gasification of wood powder*. Luleå tekniska universitet.
FU, S., LAUNDER, B., LESCHZINER, M., 1987. *Modelling strongly swirling recirculating jet flow with Reynolds-stress transport closures*, 6th Symposium on Turbulent Shear Flows, pp. 17-16.
GHADIRIAN, M., AFACAN, A., HAYES, R.E., MMBAGA, J.P., MAHMOOD, T., XU, Z., MASLIYAH, J., 2015. *A Study of the Hydrocyclone for the Separation of Light and Heavy Particles in Aqueous Slurry*. The Canadian Journal of Chemical Engineering 93, 1667-1677.
GHODRAT, M., QI, Z., KUANG, S., JI, L., YU, A., 2016. *Computational investigation of the effect of particle density on the multiphase flows and performance of hydrocyclone.* Minerals Engineering 90, 55-69.
GIBSON, M., LAUNDER, B., 1978. G*round effects on pressure fluctuations in the atmospheric boundary layer.* Journal of Fluid Mechanics 86, 491-511.
GRIFFITHS, W., BOYSAN, F., 1996. *Computational fluid dynamics (CFD) and empirical modelling of the performance of a number of cyclone samplers*. Journal of Aerosol Science 27, 281-304.
GUPTA, R., KAULASKAR, M.D., KUMAR, V., SRIPRIYA, R., MEIKAP, B.C., CHAKRABORTY, S., 2008. S*tudies on the understanding mechanism of air core and vortex formation in a hydrocyclone.* Chem Eng J 144, 153-166.
HARARAH, M.A., ENDRES, E., DUECK, J., MINKOV, L., NEESE, T., 2010. F*low conditions in the air core of the hydrocyclone*. Miner Eng 23, 295-300.
HIRSCH, C., 2007. *Numerical computation of internal and external flows: The fundamentals of computational fluid dynamics*. Butterworth-Heinemann.
HIRT, C.W., NICHOLS, B.D., 1981. *Volume of fluid (VOF) method for the dynamics of free boundaries.* Journal of computational physics 39, 201-225.
HOQUE, M.M., MITRA, S., SATHE, M.J., JOSHI, J.B., EVANS, G.M., 2016. *Experimental investigation on modulation of homogeneous and isotropic turbulence in the presence of single particle using time-resolved PIV*. Chemical Engineering Science 153, 308-329.
HSIEH, K., RAJAMANI, R., 1991. *Mathematical model of the hydrocyclone based on physics of fluid flow.* AIChE Journal 37, 735-746.
HWANG, K.J., HWANG, Y.W., YOSHIDA, H., 2013. *Design of novel hydrocyclone for improving fine particle separation using computational fluid dynamics*. Chemical Engineering Science 85, 62-68.
JIANZHONG, C., LIJUAN, S., CHUANZHEN, W., 2016. *Desliming performance of the three-product cyclone classification screen.* Journal of China University of Mining&Technology 45, 807-813. (China)
KARNIADAKIS, G., SHERWIN, S., 2013. *Spectral/hp element methods for computational fluid dynamics.* Oxford University Press.
LAUNDER, B., REECE, G.J., RODI, W., 1975. *Progress in the development of a Reynolds-stress turbulence closure*. Journal of fluid mechanics 68, 537-566.
LAUNDER, B.E., 1989a. *Second-moment closure: present… and future?* International Journal of Heat and Fluid Flow 10, 282-300.
LAUNDER, B.E., 1989b. S*econd-moment closure and its use in modelling turbulent industrial flows.* International Journal for Numerical Methods in Fluids 9, 963-985.
LI, Q., XU, W., WANG, J., JIN, Y., 2015. *Performance evaluation of a new cyclone separator–Part I experimental results.* Separation and Purification Technology 141, 53-58.
LI, X., XU, H., LIU, J., Zhang, J., LI, J., GUI, Z., 2016. *Cyclonic state micro-bubble flotation column in oil-in-water emulsion separation.* Separation and Purification Technology 165, 101-106.
LIU, Y., YANG, Q., QIAN, P., WANG, H.L., 2014. *Experimental study of circulation flow in a light dispersion hydrocyclone*. Separation and Purification Technology 137, 66-73.
LIU, Z., JIAO, J., ZHENG, Y., ZHANG, Q., JIA, L., 2006. *Investigation of turbulence characteristics in a gas cyclone by stereoscopic PIV*. AIChE journal 52, 4150-4160.
LIU, Z., ZHENG, Y., JIA, L., ZHANG, Q., 2007. A*n experimental method of examining three-dimensional*

swirling flows in gas cyclones by 2D-PIV. Chemical Engineering Journal 133, 247-256.

MAINZA, A., NARASIMHA, M., POWELL, M.S., HOLTHAM, P.N., BRENNAN, M., 2006. *Study of flow behaviour in a three-product cyclone using computational fluid dynamics*. Minerals Engineering 19, 1048-1058.

MARINS, L., DUARTE, D., LOUREIRO, J., MORAES, C., FREIRE, A.S., 2010. *LDA and PIV characterization of the flow in a hydrocyclone without an air-core*. Journal of Petroleum Science and Engineering 70, 168-176.

MOTIN, A., BENRAD, A., 2017. *Design of liquid–liquid separation hydrocyclones using parabolic and hyperbolic swirl chambers for efficiency enhancement*. Chemical Engineering Research and Design 122, 184-197.

MOUSAVIAN, S., NAJAFI, A., 2009. *Numerical simulations of gas--liquid--solid flows in a hydrocyclone separator*. Archive of Applied Mechanics(Ingenieur Archiv) 79, 395-409.

NARASIMHA, M., SRIPRIYA, R., BANERJEE, P., 2005. *CFD modelling of hydrocyclone – prediction of cut size*. International Journal of Mineral Processing 75, 53-68.

NIAZI, S., HABIBIAN, M., RAHIMI, M., 2017. *Performance evaluation of a uniflow mini-hydrocyclone for removing fine heavy metal particles from water*. Chemical Engineering Research and Design 126, 89-96.

OBENG, D., MORREL, S., 2003. T*he JK three-product cyclone – performance and potential applications.* International journal of mineral processing 69, 129-142.

PARVAZ, F., HOSSEINI, S.H., AHMADI, G., ELSAYED, K., 2017. *Impacts of the vortex finder eccentricity on the flow pattern and performance of a gas cyclone*. Separation and Purification Technology 187, 1-13.

QUIAN, L., CHANGLIE, D., JIRUN, X., LIXIN, Y., GUANGAI, X., 1989. C*omparison of the performance of water-sealed and commercial hydrocyclones*. International Journal of Mineral Processing 25, 297-310.

ROLDAN-VILLASANA, E., WILLIAMS, R., DYAKOWSKI, T., 1993. T*he origin of the fish-hook effect in hydrocyclone separators*. Powder Technology 77, 243-250.

SALEM-SAID, A.-H., FAYED, H., RAGAB, S., 2013. *Numerical simulations of two-phase flow in a Dorr-Oliver flotation cell model.* Minerals 3, 284-303.

SANTANA, R.C., FARNESE, A.C., FORTES, M.C., ATAIDE, C.H., BARROZO, M.A., 2008. *Influence of particle size and reagent dosage on the performance of apatite flotation*. Separation and Purification Technology 64, 8-15.

SCHUETZ, S., MAYER, G., BIERDEL, M., PIESCHE, M., 2004. *Investigations on the flow and separation behaviour of hydrocyclones using computational fluid dynamics.* International Journal of Mineral Processing 73, 229-237.

SLACK, M., WRAITH, A., 1997. *Modelling the velocity distribution in a hydrocyclone*, 4th International Colloquium on Process Simulation, pp. 65-83.

SOLERO, G., COGHE, A., 2002. *Experimental fluid dynamic characterization of a cyclone chamber*. Experimental thermal and fluid science 27, 87-96.

SVAROVSKY, L., THEW, M., 1992. *Hydrocyclones: analysis and applications.* Springer Science & Business Media.

SWAIN, S., MOHANTY, S., 2013. *A 3-dimensional Eulerian–Eulerian CFD simulation of a hydrocyclone*. Applied Mathematical Modelling 37, 2921-2932.

VAKAMALLA, T.R., MANGADODDY, N., 2017. *Numerical simulation of industrial hydrocyclones performance: Role of turbulence modelling*. Separation and Purification Technology 176, 23-39.

VIEIRA, L.G., SILVA, D.O., BARROZO, M.A., 2016. *Effect of Inlet Diameter on the Performance of a Filtering Hydrocyclone Separator*. Chemical Engineering & Technology 39, 1406-1412.

VIEIRA, L.G.M., BARROZO, M.A.S., 2014. *Effect of vortex finder diameter on the performance of a novel hydrocyclone separator.* Minerals Engineering 57, 50-56.

VIEIRA, L.G.M., DAMASCENO, J.J.R., BARROZO, M.A.S., 2010. I*mprovement of hydrocyclone separation performance by incorporating a conical filtering wall*. Chem Eng Process 49, 460-467.

WANG, B., CHU, K., YU, A., 2007. *Numerical Study of Particle− Fluid Flow in a Hydrocyclone*. Industrial & engineering chemistry research 46, 4695-4705.

WANG, B., YU, A., 2006. *Numerical study of particle–fluid flow in hydrocyclones with different body dimensions.* Miner Eng 19, 1022-1033.

WANG, C., CHEN, J., SHEN, L., HOQUE, M.M., GE, L., EVANS, G.M., 2018. *Inclusion of screening to*

remove fish-hook effect in the three products hydro-cyclone screen (TPHS). Minerals Engineering 122, 156-164.

WANG, J., BAI, Z., YANG, Q., FAN, Y., WANG, H., 2016. *Investigation of the simultaneous volumetric 3-component flow field inside a hydrocyclone.* Separation and Purification Technology 163, 120-127.

WASILEWSKI, M., 2016. *Analysis of the effects of temperature and the share of solid and gas phases on the process of separation in a cyclone suspension preheater*. Separation and Purification Technology 168, 114-123.

WILCOX, D.C., 1998. *Turbulence modeling for CFD*. DCW industries La Canada, CA.

XU, W., LI, Q., WANG, J., JIN, Y., 2016. *Performance evaluation of a new cyclone separator–Part II simulation results.* Separation and Purification Technology 160, 112-116.

YOSHIDA, H., YOSHIKAWA, S., FUKUI, K., YAMAMOTO, T., 2008. *Effect of multi-inlet flow on particle classification performance of hydro-cyclones.* Powder Technology 184, 352-360.

ZHEN-BO, W., YI, M., YOU-HAI, J., 2011. *Simulation and experiment of flow field in axial-flow hydrocyclone.* Chemical Engineering Research & Design 89, 603-610.

ZHU, X.-b., XU, N.-x., LIU, L.-h., 2012. *Application of three-product cyclone sizing screen in classification and thickening of slime in Xuehu coal preparation plant.* Coal Preparation Technology 1, 012. (China)